Journal of Algorithms and Computations

journal homepage: http://jac.ut.ac.ir

Comparative Analysis of Second-Order Unconstrained Iterative Solvers for Non-Linear Inversion of Finite-Element Based DC Resistivity Simulation

A.Yazdanpanah[1] and M. Abedi[*1]

[1] Petroleum Engineering and Geophysics Laboratory, School of Mining Engineering, College of Engineering, University of Tehran, Iran

ABSTRACT

Direct Current (DC) Electrical Resistivity Tomography (ERT) inversion is a non-linear, ill-posed problem requiring robust solvers for accurate subsurface resistivity reconstruction. This study systematically compares four second-order iterative solvers: Simple Newton, Newton-CG, Trust-Exact, and Trust-NCG, using synthetic dipole-dipole data with conductive and resistive anomalies in a homogeneous background. Inversion is performed within a finite-element framework with unstructured triangular meshes. Results show Newton-CG, Trust-Exact, and Trust-NCG converge reliably, while Trust-Exact and Trust-NCG are superior in resolving sharp resistivity contrasts owing to adaptive trust-region globalization. Newton-CG and Trust-NCG exhibit minor smoothing, reflecting a trade-off between speed and precision. These findings highlight the superiority of trust-region methods in weakly regularized non-linear geophysical inversion.

Keywords: Direct Current, Electrical Resistivity Tomography (ERT), Inversion, Finite-Element

ARTICLE INFO

Article history:
Research paper
Received 11, October 2025
Accepted 01, December 2025
Available online 28, December 2025

AMS subject classification: 49M15

[*] Corresponding author: M. Abedi

Email: maysamabedi@ut.ac.ir.

1 Introduction

Direct Current (DC) Electrical Resistivity Tomography (ERT) is a geophysical imaging technique that reconstructs subsurface electrical resistivity distributions from surface or near-surface measurements. Widely applied in environmental and engineering studies, ERT enables the non-invasive detection of geological features such as groundwater aquifers, fracture zones, and contamination plumes [1]. Mathematically, ERT inversion is a large-scale, non-linear, ill-posed optimization problem, making it a compelling testbed for evaluating advanced numerical algorithms [2]. This study, presented in the context of computational optimization, systematically compares four second-order unconstrained iterative solvers encompassing Simple Newton, Newton-CG, Trust-Exact, and Trust-NCG, to enhance the accuracy and efficiency of ERT inversion within a finite-element framework, addressing challenges in computational geophysics through a numerical view.

The non-linear relationship between measured apparent resistivities and subsurface resistivity distributions poses significant computational challenges. ERT inversion seeks to minimize a objective function with Tikhonov regularization for model norm, balancing a data misfit term, which quantifies discrepancies between observed and predicted data, with a regularization term to mitigate ill-posedness [3]. The regularization parameter, scaled by a dimensionless factor, controls the trade-off between data fidelity and model smoothness [4]. This study employs synthetic data generated via a dipole-dipole electrode array, a configuration chosen for its balance of lateral resolution and depth sensitivity, to evaluate solver performance under controlled conditions [5]. By focusing on unconstrained solvers, we aim to explore their flexibility in handling complex subsurface models without explicit parameter bounds, a critical aspect for high-dimensional inverse problems.

Traditional ERT inversion often relies on commercial software implementing variants of Gauss-Newton or conjugate gradient methods with regularization. While effective for standard scenarios, these approaches may struggle with noisy datasets or complex geological structures, leading to non-unique solutions or convergence to local minima [6]. The computational burden is exacerbated by the need to solve large-scale linear systems at each iteration, derived from linearizing the non-linear forward mapping [7]. This research investigates second-order solvers that leverage gradient and Hessian information to navigate the non-convex optimization landscape, aiming to identify strategies that improve robustness and computational efficiency for practical ERT applications.

The forward modeling stage of ERT, critical to inversion, involves simulating electrical potential fields in a discretized subsurface domain [8]. This study uses the PyGIMLi framework [9], employing finite-element methods (FEM) to model complex geometries and resistivity variations accurately. The FEM approach discretizes the subsurface into a computational mesh, enabling precise prediction of apparent resistivities. By generating synthetic data with a controlled dipole-dipole configuration, we ensure a consistent basis for comparing solver performance, focusing on their ability to reconstruct sharp resistivity contrasts in the presence of very weak regularization.

A key aspect of the forward modeling process is the meshing strategy. This study adopts unstructured triangular meshing, which offers computational efficiency through fewer nodes per

element compared to structured rectangular grids. Unstructured meshes provide superior geometric flexibility, allowing local refinement near electrode positions and anomalous regions, thus reducing numerical approximation errors [10]. This approach is particularly advantageous for handling the irregular boundaries and heterogeneous resistivity distributions common in geophysical applications, ensuring accurate forward simulations that underpin the inversion process.

This research contributes to the field of numerical algorithms by offering a rigorous comparison of second-order unconstrained solvers for ERT inversion. The findings guide the selection of optimal methods for balancing solution quality and computational cost, with implications for both geophysical applications and broader scientific computing challenges. By highlighting the strengths and weaknesses of each solver, particularly the limitations of fixed-step methods, this study provides actionable recommendations for practitioners and researchers tackling large-scale, non-linear inverse problems in computational geophysics and beyond.

2 Finite-Element Simulation

This section details the Finite Element (FE) methodology for simulating DC Resistivity data, generating predicted apparent resistivities for inversion. Current is injected through a pair of current electrodes (A and B, or C1 and C2), with voltage measured across potential electrodes (M and N, or P1 and P2) using a dipole-dipole array configuration. The apparent resistivity is calculated as:

$$\rho_a = K\frac{\Delta V}{I} = \pi n(n+1)(n+2)a\frac{\Delta V}{I},$$

where n is the dipole separation factor, a is the electrode spacing within a dipole, ΔV is the measured voltage, and I is the injected current. The geometric factor K adjusts for the array's configuration, ensuring accurate resistivity estimates [1]. Figure 1a illustrates the dipole-dipole array setup, with the midpoint centered between dipoles for data interpretation.

This section outlines the FE methodology for simulating ERT data, generating predicted apparent resistivities for inversion. The following sections formulate the boundary value problem governing the electrical potential distribution, address singularities at electrode positions by decomposing the potential into primary and secondary components, and describe the numerical solution of the resulting sparse linear systems, leveraging their symmetry and sparsity. Together, these components establish a robust framework for generating synthetic ERT data to evaluate second-order unconstrained solvers. Figure 1b depicts a detailed flowchart of the implemented methodology in this study.

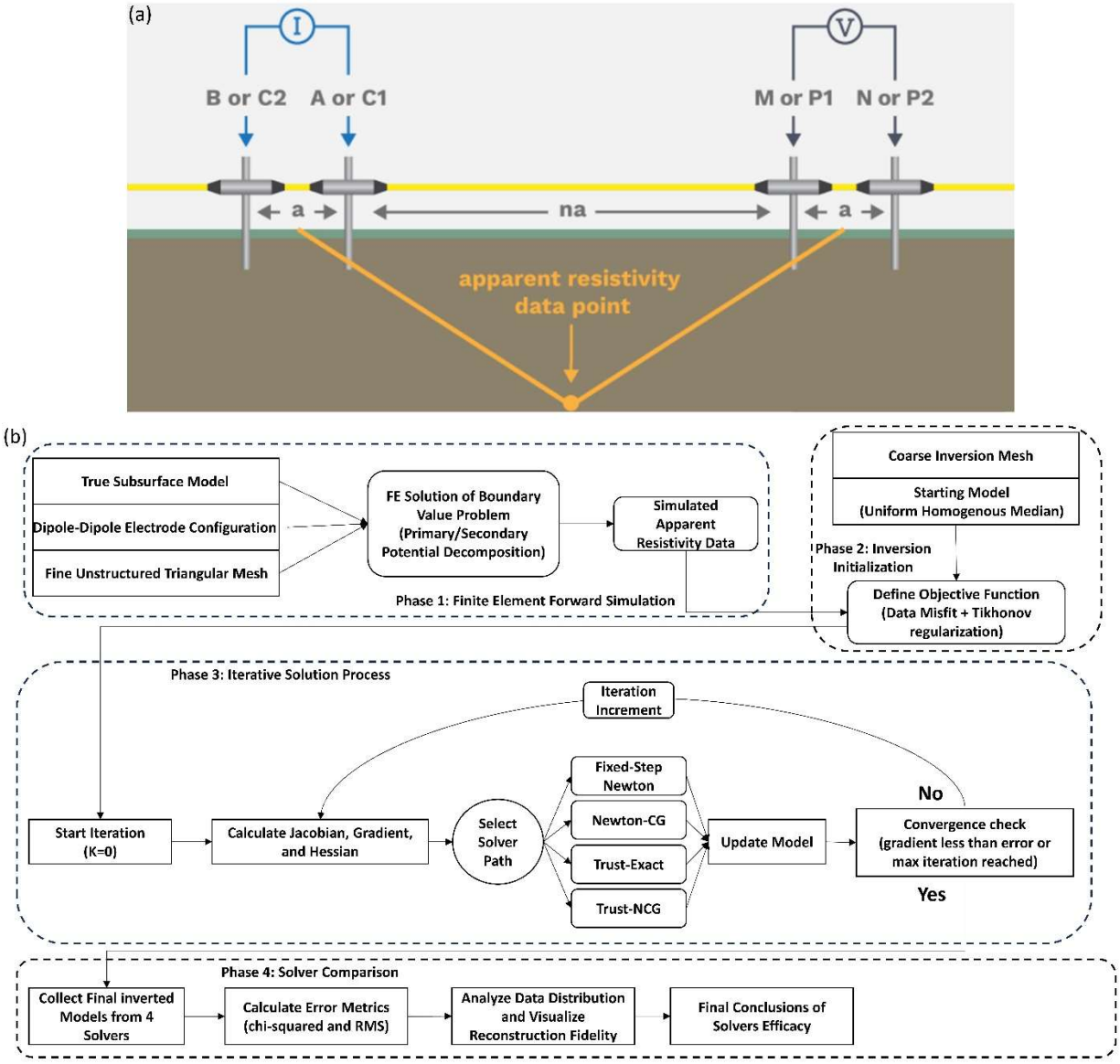

Figure 1: (a) A schematic illustrating the data acquisition of a geoelectrical survey using Dipole-Dipole electrode array, (b) Flowchart of phases conducted in this study.

2.1 Total Potential Calculation

The electrical potential distribution is modeled by solving a boundary value problem derived from the continuity equation, with generalized boundary conditions for current injection at electrodes A and B (or C1 and C2) and surface effects. The governing equation is expressed as:

$$\nabla.(\sigma \nabla u) = -\nabla.j \; in \; \Omega \subset R^2,$$

$$\sigma\left(\frac{\partial u}{\partial n} + \alpha u\right) = j.n \; on \; \Gamma = \Gamma_s \cup \Gamma_E$$

where $\sigma(x,z)$ denotes the conductivity distribution, j is the source current density, u represents the electrical potential, n is the outward normal vector on the boundary, and α is a boundary condition parameter. Current I is injected via point-like electrodes at positions $\mathrm{r}_s = (x_s, y_s)$, modeled as $\nabla \cdot \mathrm{j} = I\delta(\mathrm{r} - \mathrm{r}_s)$, with δ being the Dirac delta function. Neumann conditions ($\alpha = 0$) are applied at the surface boundary Γ_s to prevent current flow outward, while mixed boundary conditions ($\alpha = \mathrm{n} \cdot \mathrm{r}/|\ \mathrm{r}\ |^2$) are used elsewhere, following [11], for mathematical precision and flexible electrode placement.

Applying the weighted residual method, as described by [12], yields the weak form of the boundary value problem:

$$\int_{\Omega} \sigma . \nabla w \nabla u \, d\Omega + \int_{\Gamma} \sigma \alpha w u \, d\Gamma = \int_{\Omega} wI\delta(r - r_s) \, d\Omega + \int_{\Gamma} wj.n \, d\Gamma$$

where w represents a set of weighting functions. This formulation supports piecewise approximation of u, requiring only first derivatives, which enhances numerical stability. The subsurface domain is discretized into distinct elements, leading to a linear system $\mathrm{Au} = \mathrm{b}$, where $\mathrm{A} \in \mathbb{R}^{N \times N}$is a symmetric, positive definite, sparse matrix with N nodes, u contains the nodal potentials, and b encapsulates source terms.

2.1 Calculation of the Secondary Potential

The Dirac delta function in the source term introduces a singularity at electrode positions, causing steep potential gradients that degrade numerical accuracy near r_s. To mitigate this, the potential is decomposed into primary u_p and secondary u_s components, $u = u_p + u_s$ [13]. The secondary potential is governed by:

$$\nabla \cdot (\sigma \nabla u_s) = \nabla \cdot \left((\sigma_p - \sigma) \nabla u_p \right) \ in\ \Omega,$$

$$\sigma\left(\frac{\partial u_s}{\partial n} + \alpha u_s\right) = (\sigma_p - \sigma)\left(\frac{\partial u_p}{\partial n} + \alpha u_p\right) \ \text{on}\ \Gamma,$$

where σ_p is the conductivity at the electrode's immediate vicinity, ensuring regularity of the primary potential gradient. This approach eliminates the singular current density, with secondary sources arising where σ deviates from σ_p. The system is expressed as:

$$A^{\sigma} u_s = A^{\sigma_p - \sigma} u_p$$

where $\mathrm{A}^{\sigma}$and $\mathrm{A}^{\sigma_p - \sigma}$are matrices corresponding to the conductivity distributions. To optimize computation, the linearity of A is exploited like below:

$$A^{\sigma_p - \sigma} u_p = (A^{\sigma_p} - A^{\sigma}) u_p = A^1 u_p \sigma_p - A^{\sigma} u_p$$

requiring only one additional matrix A^1 for a homogeneous conductivity of 1, alongside A^{σ}, for all source calculations [14].

2.3 Solving the System of Equations

The forward simulation solves the linear system $\mathrm{A}u_l = \mathrm{b}_l$ for each current source $l = 1, \ldots, E$, where $E = 51$ electrodes are positioned along the x-axis from 0 to 50 m. The subsurface model includes two anomalies: a conductive circular anomaly (50 Ω·m, radius 5 m, centered at (10, -7) m) and a resistive rectangular anomaly (350 Ω·m, spanning x = 35 to 50 m and y = -10 to -20 m), set against a background resistivity of 200 Ω·m. These anomalies create a general scenario to challenge the inversion process. A high-quality mesh with cell areas of approximately 1 m², generated through delaunay triangulation, ensures precise capture of resistivity variations in the simulated data. The matrix A is symmetric and sparse, with 3 to 20 non-zero entries per row (average of 14) using linear shape functions. Potentials are computed for individual electrodes and superposed to enhance efficiency, as electrodes are reused across measurements. This approach provides accurate predicted data for subsequent inversion, leveraging the fine mesh to resolve subtle variations in the complex subsurface model while decreasing the required computations. Figure 2 illustrates the forward simulation outcomes where part (a) shows the primary assumed geometry comprising one circular conductive and one rectangular resistive anomalies and part (b) depicts the pseudo-section of simulated apparent data. This can be inferred that the simulation has better captured the conductive anomaly compared to the resistive one. It can be because of the anomaly location and the sensitivity of utilized array here in this study.

3 Inverse Modeling and Results

The goal of ERT inversion is to reconstruct the subsurface resistivity distribution by minimizing an objective function that balances data misfit with model regularization. The objective function is expressed as:

$$\varphi(m_k) = (d - f(m_k)^T C_d^{-1}(d - f(m_k))^T + \lambda m_k^T W^T W_m$$

where d denotes the observed apparent resistivities (in logarithmic form), $\mathrm{f}(\mathrm{m}_k)$ represents the forward model predictions, $\mathrm{C}_d^{-1}$is the inverse data covariance matrix, W_m is the model smoothing matrix, m_k is the model vector of logarithmic resistivities at iteration k, and λ is the regularization parameter with an optimal value of 0.0001 in this study. The model update is computed as:

$$\Delta m = H(m_k).\nabla\varphi(m_k)$$

with the Hessian $H(m_k)$ like:

$$H(m_k) = (J^T C_d^{-1} J + \lambda W^T W_m)^{-1}$$

And the Gradient:

$$\nabla\varphi(m_k) = \left(J^T C_d^{-1}\left(d - f(m)\right) + \lambda W^T W_m m\right)$$

Where the Jacobian J is defined as:

$$J_{i,j} = \partial F_i / \partial m_j$$

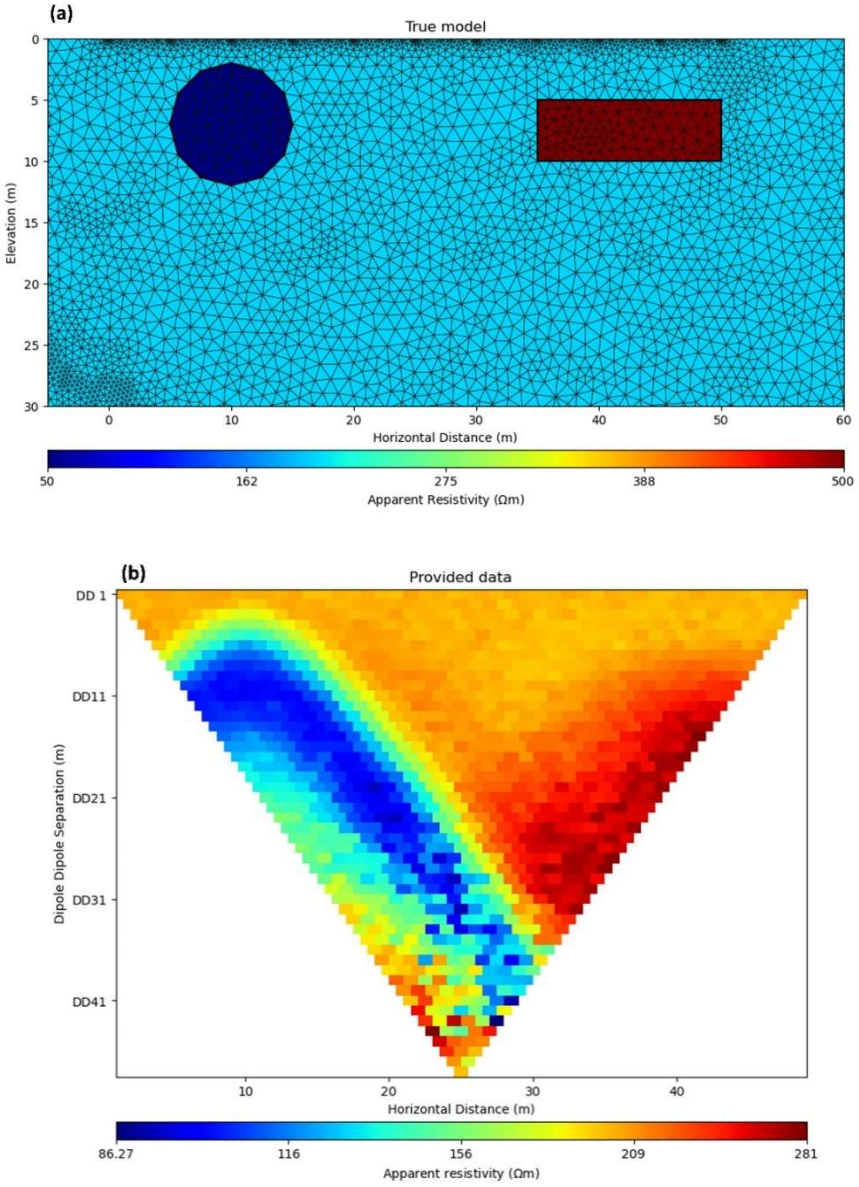

Figure 2: DC resistivity forward modeling results; (a) True subsurface resistivity model, featuring a conductive circular anomaly and a resistive rectangular anomaly, overlaid with the Delaunay triangulation-based unstructured mesh; (b) Pseudo-section of simulated apparent resistivity data obtained using the dipole-dipole configuration.

Iterations proceed until convergence, achieved when the gradient norm falls below a threshold (e.g., 10^{-4}) or a maximum number of iterations (5, in this study) is reached, ensuring the model aligns with observed data while maintaining smoothness. This study investigates unconstrained iterative solvers to identify optimal approaches for 2D resistivity reconstruction in synthetic geophysical settings. The choice of iterative solver critically dictates how accurately and efficiently this system is solved and how the resulting step length is controlled to ensure global convergence [15].

The non-linearity of ERT inversion, driven by the complex relationship between apparent resistivities and subsurface properties, necessitates iterative solvers to navigate the non-linear objective function. Unconstrained solvers, which allow unrestricted model parameter exploration, provide flexibility and simplicity for diverse geological scenarios but risk converging to local minima or sensitivity to initial model choices. Their strengths include ease of implementation and adaptability across problem scales, while drawbacks include potential instability without careful regularization. This research evaluates multiple unconstrained solvers to determine their efficacy in achieving accurate and numerically efficient subsurface resistivity models.

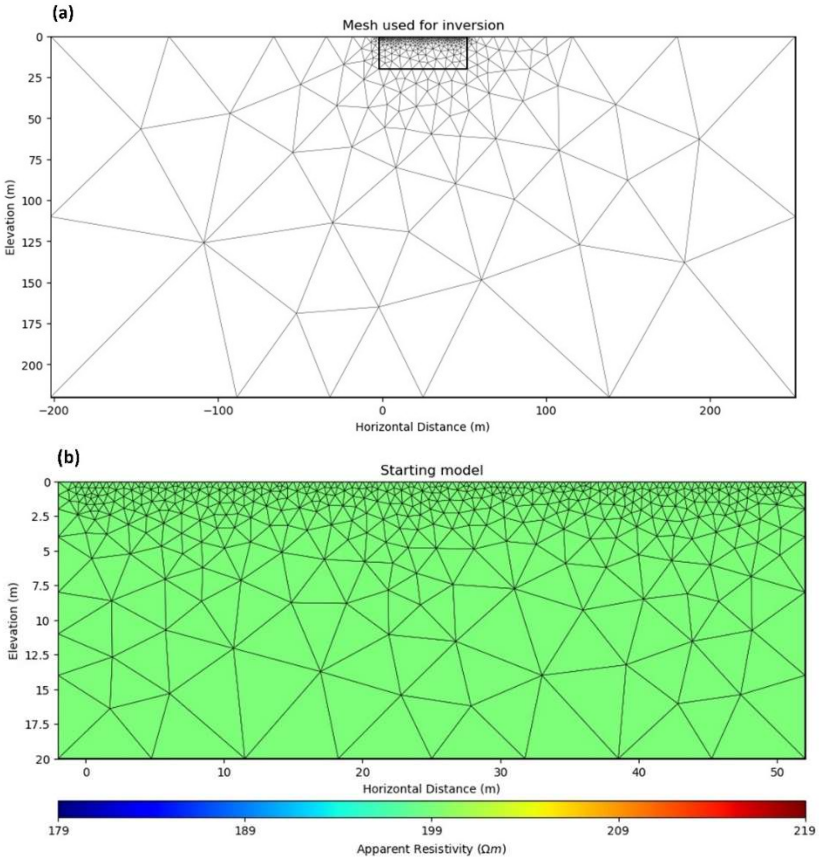

Figure 3: Inversion setup: (a) Unstructured triangular inversion mesh; (b) Starting resistivity model for all solvers.

For this study, an unstructured triangular inversion mesh is utilized, covering $x = -5$ to 60 m and $y = -30$ to 0 m. This mesh, with 1031 cells, is coarser than the forward simulation mesh (cell area ~1 m²) to enhance computational efficiency, accommodating standard computing resource limitations. The synthetic model's controlled complexity, featuring two anomalies, does not necessitate a finer inversion mesh, as the triangular mesh adequately supports the comparison of solver performance. The starting model, initialized with a uniform resistivity equal to the median of the observed apparent resistivities, is consistently applied across all solvers to ensure a fair evaluation. Figure 3 illustrates the unstructured triangular inversion mesh, highlighting its coarse structure, and the starting model, showing the initial uniform resistivity distribution for all methods.

3.1 Fixed-Step Newton Method

The fixed-step Newton method offers a simple approach to ERT inversion, updating model parameters with a constant step length to minimize computational complexity compared to adaptive methods like line search or trust-region techniques [16]. While straightforward, its fixed step ($\alpha = 0.01$) may limit convergence speed and accuracy in intricate resistivity distributions. Unlike Gauss-Newton methods, which approximate the Hessian for least-squares problems like ERT, this method uses the full Hessian, including second derivatives, making it more general but computationally demanding. The update is given by:

$$m_{k+1} = m_k - \alpha[H(m_k)]^{-1}\nabla\varphi(m_k)$$

where m_k is the model vector of logarithmic resistivities at iteration k. Figure 4 illustrates the method's outcomes. The inferred resistivity model, depicting the reconstructed subsurface structure, and the response data pseudo-section, showing predicted apparent resistivities, which can be compared to the simulated data in Figure 2(b).

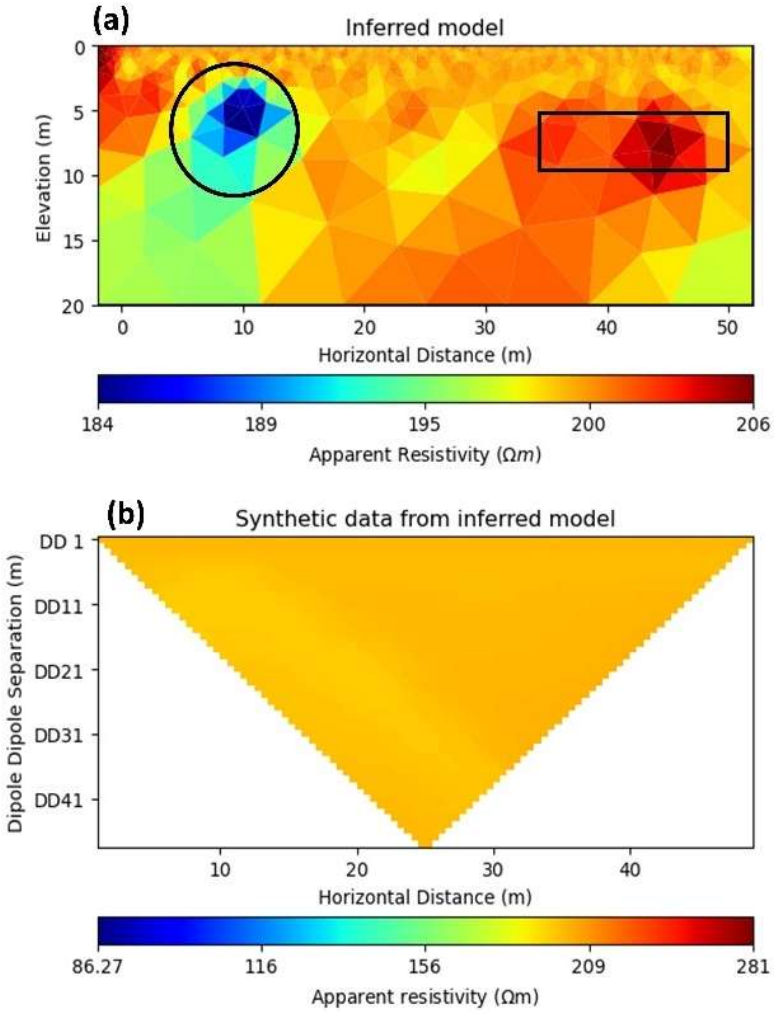

Figure 4: Inversion results for fixed-step Newton method; (a) Inferred model; and (b) Response data from inferred model.

3.2 Newton Conjugate Gradient Method

The Newton-Conjugate Gradient (Newton-CG) method, a refinement of the classical Newton approach, approximates the inverse of the Hessian matrix using an iterative conjugate gradient solver, enhancing computational efficiency for large-scale problems [17]. In the context of this study, Newton-CG is applied to the non-linear ERT inversion problem within the PyGIMLi framework, minimizing a Tikhonov-regularized objective function for synthetic dipole-dipole data. The method approximates the objective function locally as a quadratic form:

$$f(x) \approx f(x_0) + \nabla f(x_0).(x - x_0) + \frac{1}{2}(x - x_0)^T H(x_0)(x - x_0)$$

where $H(x_0)$ represents the Hessian matrix of second derivatives. For a positive definite Hessian, the local minimum is obtained by solving the linear system derived from setting the quadratic form's gradient to zero:

$$x_{opt} = x_0 - H^{-1}\nabla f$$

In the Newton-CG method, the Hessian's inverse is approximated efficiently via the conjugate gradient algorithm, avoiding explicit matrix inversion. To leverage the efficiency of the Newton-CG method, a function computing the Hessian-vector product is supplied, eliminating the need to form the full Hessian matrix explicitly. This approach reduces computational cost, particularly for the high-dimensional systems in ERT, and provides a robust alternative to Simple Newton's fixed-step approach, The exact Hessian inversion of Trust-Exact, and the Krylov-based approximation of Trust-NCG, as assessed in our comparative analysis. This method approximates the search direction p_k by solving:

$$\mathrm{H}(\mathrm{m}_k)\mathrm{p}_k = -\nabla\varphi(\mathrm{m}_k)$$

via conjugate gradient iterations, which is particularly efficient for large Hessians in ERT inversion. The line search ensures descent by satisfying Wolfe conditions, balancing computational cost with adaptability to complex resistivity distributions. The update is formulated as:

$$\mathrm{m}_{k+1} = \mathrm{m}_k + \alpha_k \mathrm{p}_k$$

where p_k is the conjugate gradient direction, and α_k is selected to minimize ϕ along the line, typically via backtracking or strong Wolfe conditions ($c_1 = 10^{-4}$, $c_2 = 0.9$) [18]. The resulted outputs from this method are illustrated in figure 5 showing a much better model and data response than the fixed-step method.

3.3 Nearly Exact Trust Region Method

The Nearly Exact Trust-Region method enhances ERT inversion by limiting model updates within a trust region, ensuring robust convergence for non-linear problems. This approach solves a quadratic subproblem to find the step p_k that minimizes the quadratic approximation of the objective function $\varphi(\mathrm{m}_k)$ within a trust-region radius Δ_k. The update is given by:

$$\mathrm{m}_{k+1} = \mathrm{m}_k + \mathrm{p}_k, \text{s.t.} \parallel \mathrm{p}_k \parallel \leq \Delta_k$$

where p_k minimizes

$$q(\mathrm{p}) = \varphi(\mathrm{m}_k) + \nabla\varphi(\mathrm{m}_k)^T\mathrm{p} + \frac{1}{2}\mathrm{p}^T\mathrm{H}(\mathrm{m}_k)\mathrm{p}$$

The radius Δ_k is adjusted based on the ratio of actual to predicted reduction in φ, ensuring steps remain reliable. This method excels in handling the non-linearities of ERT inversion, particularly for the synthetic model with conductive and resistive anomalies, by limiting step sizes to regions where the quadratic model is accurate [19]. In this study, the method achieves convergence in 5 iterations. It relatively resolves both anomalies with stable parameter updates (Figure 6).

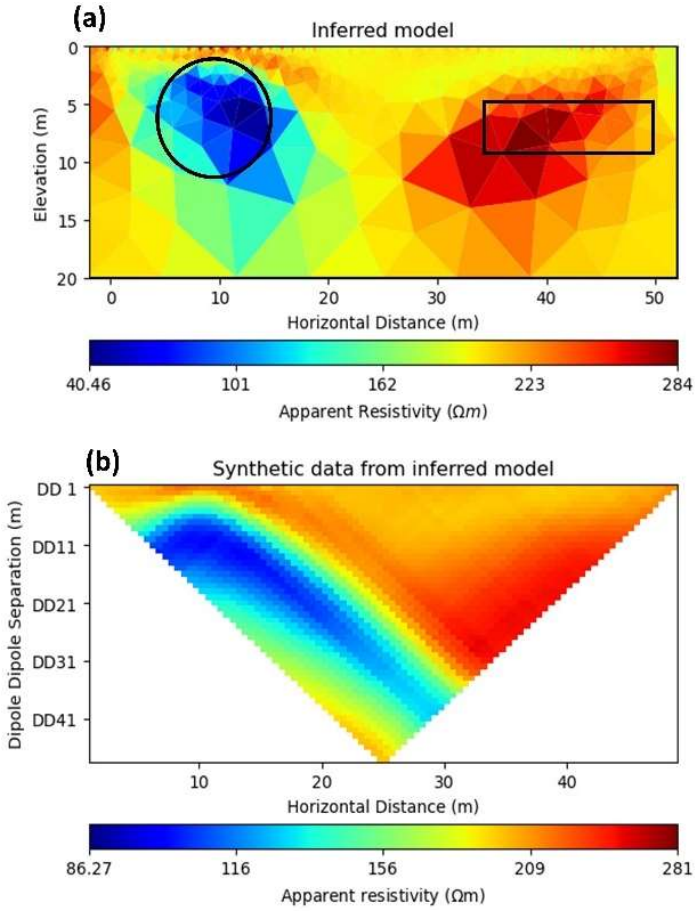

Figure 5: Inversion results for Newton conjugate gradient method; (a) Inferred model; and (b) Response data from inferred model.

3.5 Newton Conjugate Gradient Trust Region Method

The Newton Conjugate Gradient Trust-Region (Trust-NCG) method refines ERT inversion by combining trust-region constraints with conjugate gradient iterations, incorporating adaptive step adjustments for robust convergence. The model update is exactly expressed like the trust-exact method [20].

This hybrid approach balances computational efficiency and stability, effectively handling the non-linearities of the synthetic ERT model with conductive and resistive anomalies. The Rosenbrock function, used previously, underscores its capability to navigate complex optimization landscapes (Figure 7).

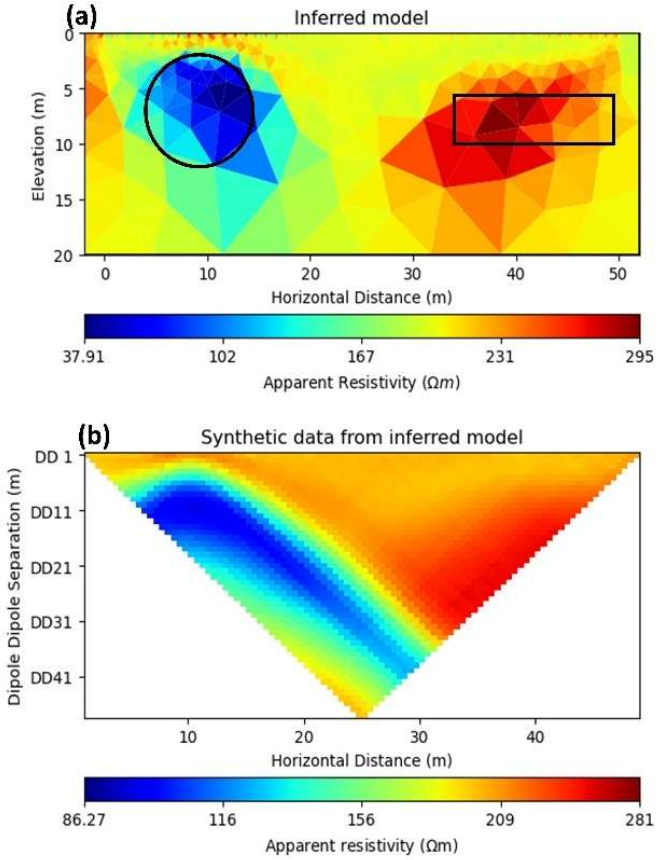

Figure 6: Inversion results for trust-exact method; (a) Inferred model; and (b) Response data from inferred model.

4 Comparison of the Results

Visual inspection of inferred resistivity models and their corresponding data provides limited insight into the performance of inversion solvers, as qualitative assessments alone cannot capture the quantitative differences critical for rigorous comparison. To address this, we analyze the data distributions of the reconstructed models alongside error metrics, specifically χ_N^2 and relative root-mean-square (RMS) error, to evaluate the performance of Simple Newton, Newton-CG, Trust-Exact, and Trust-NCG solvers for synthetic dipole-dipole ERT data. The χ_N^2 metric quantifies the misfit between observed and predicted data, defined as:

$$\chi_N^2 = \frac{1}{N}\sum_{i=1}^{N}\left(\frac{d_i - f(m)_i}{\sigma_i}\right)^2$$

where d_i and $f(m)_i$ are observed and predicted data, respectively, and σ_i is the standard error, for the i-th datum with N data.

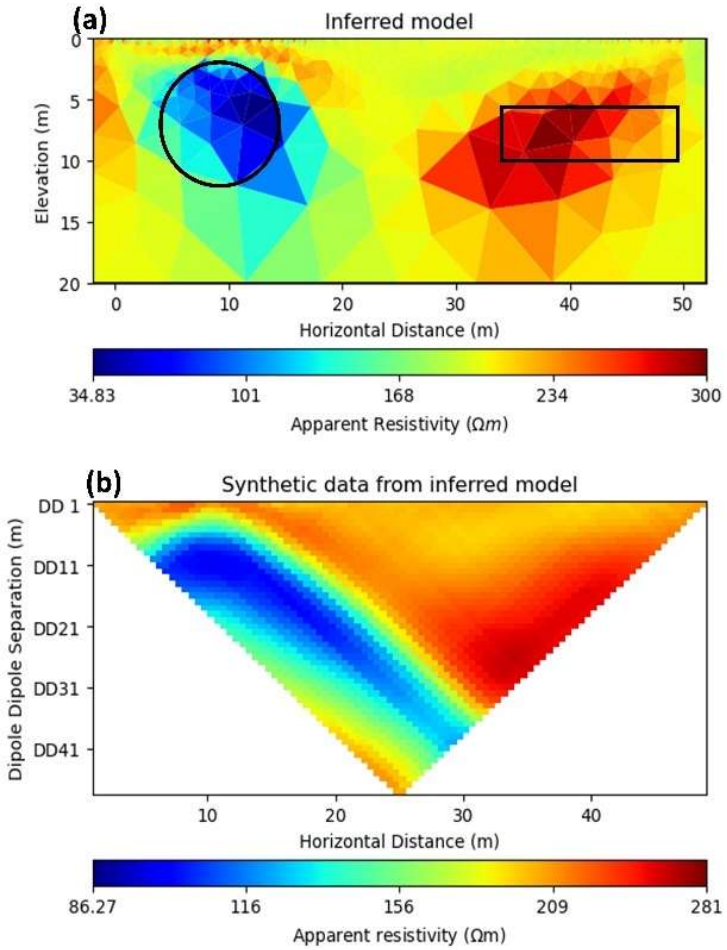

Figure 7: Inversion results for trust-exact method; (a) Inferred model; and (b) Response data from inferred model.

The RMS error evaluates the precision of ERT inversion by calculating the discrepancy between observed and predicted apparent resistivity values. For a set of N measurements, the observed resistivities d_i from synthetic dipole-dipole data are compared to predicted values $f_i(m)$, derived from the inverted resistivity model. The RMS error, computed unweighted by data uncertainties, is defined as :

$$RMS = \sqrt{1/N \sum_{i=1}^{N} \left(\frac{d_i - f_i(m)}{d_i} \right)^2}$$

where i indexes each resistivity observation and N is the number of them. This metric offers a robust measure of model accuracy, enhancing the assessment of solver performance alongside χ_N^2 and data distribution analyses in this comparative study.

The calculated data distributions and error metrics for the four solvers are presented in Figure 8, comprising two parts: part (a) displays the box plot of model resistivity distributions, and part (b)

shows the bar plot of chi-squared and RMS error values. In part (a), Simple Newton's distribution reveals poor reconstruction, capturing only the background resistivity adequately while failing to resolve both anomalies, a consequence of its fixed-step iterations leading to divergence or stagnation. In contrast, Newton-CG, Trust-Exact, and Trust-NCG produce closely aligned distributions, significantly outperforming Simple Newton by accurately capturing the conductive anomaly's sharp contrast (50 Ω·m vs. 200 Ω·m background), with the resistive anomaly (350 Ω·m) slightly less resolved due to its higher contrast. This disparity arises because the lower resistivity contrast of the conductive anomaly aligns more closely with the background, facilitating better detection across flexible solvers. Also, better captured data simulated in conductive anomaly location plays a crucial role in this. Part (b) confirms that Newton-CG, Trust-Exact, and Trust-NCG achieve lower χ_N^2 and RMS errors, reflecting their adaptive globalization strategies, unlike Simple Newton's instability.

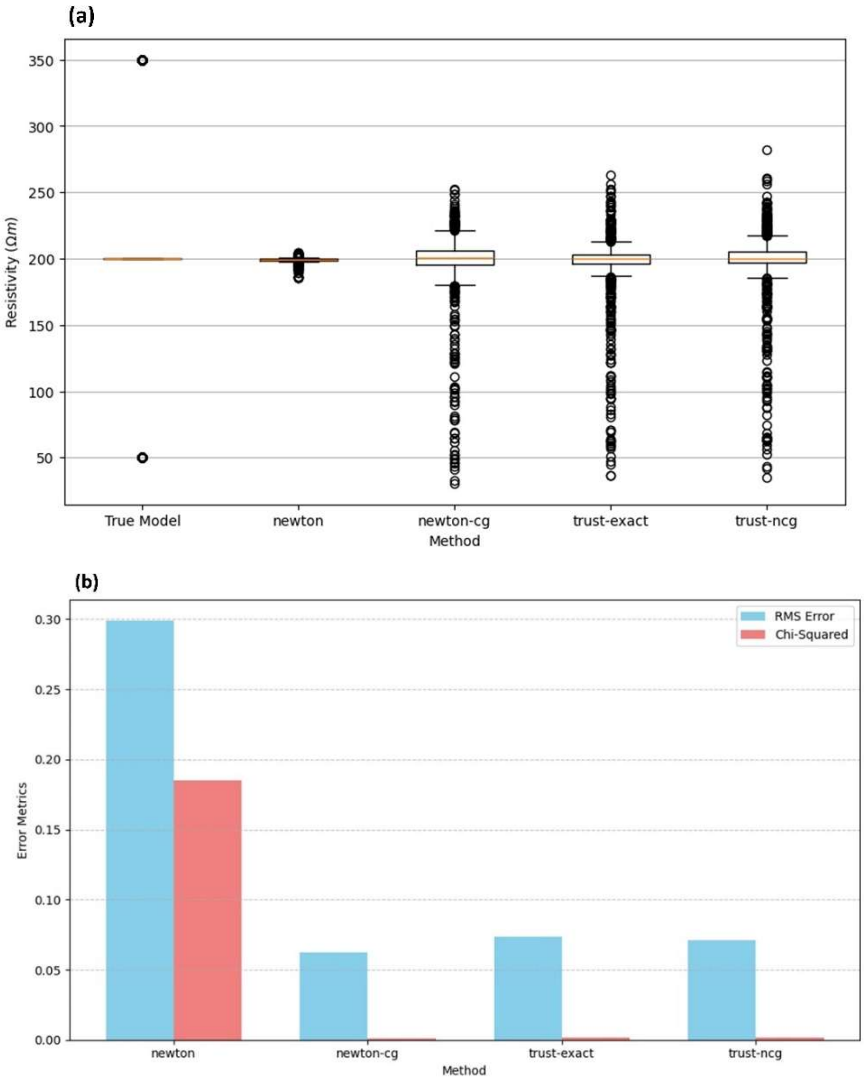

Figure 8: Comparison of the result; (a) Resistivity distribution across inversion methods and true model; and (b) Comparison of error metrics across inversion results.

The performance hierarchy underscores the critical role of globalization in achieving stable convergence for the ill-posed ERT inversion problem. Simple Newton's fixed-step approach fails due to its sensitivity to the non-convex objective function, resulting in high error metrics and blurred models. Conversely, Newton-CG's line search and Trust-Exact and Trust-NCG's trust-region strategies ensure robust descent directions, with Trust-Exact delivering the highest fidelity through precise Hessian inversion, followed closely by Trust-NCG's efficient conjugate gradient approximation. However, Newton-CG and Trust-NCG exhibit slight smoothing of the resistive anomaly, as their approximate steps rely more on regularization to stabilize iterations, unlike Trust-Exact's ability to minimize smoothing penalties. These results, visualized in Figure 8, highlight the superior balance of fidelity and efficiency in trust-region methods, offering valuable insights for optimizing non-linear geophysical inversions.

5 Conclusions

This study experimentally evaluated the performance of four unconstrained second-order solvers—Simple Newton, Newton-CG, Trust-Exact, and Trust-NCG—for non-linear ERT inversion using synthetic dipole-dipole data, revealing significant performance disparities. Trust-Exact and Trust-NCG demonstrated superior model fidelity, effectively reconstructing conductive (50 Ω·m) and resistive (350 Ω·m) anomalies against a 200 Ω·m background, owing to their robust trust-region strategies, while Simple Newton's fixed-step approach failed, and Newton-CG showed slight smoothing due to regularization reliance. In real geophysical applications, robust regularization and constrained inversion are critical to address ill-posedness, unlike the unconstrained flexibility explored here. Adjusting the true model's resistivity contrasts could further enhance results, particularly for high-contrast anomalies. Future research could explore alternative optimization methods, including constrained solvers or PyGIMLi's Gauss-Newton conjugate gradient least-squares approach, which was excluded here due to its constrained nature. Refining the inversion mesh may reduce blurring but increase computational cost, while testing solvers in complex scenarios, such as rugged topography or layered media, and exploring alternative meshing strategies could further elucidate their applicability to diverse geophysical challenges. Also, extending the 2D study to 3D is another significant and interesting challenge that can be conducted in future related studies.

Acknowledgments

We extend our heartfelt gratitude to the Faculty of Mining Engineering at the University of Tehran for their invaluable support in the execution of this research.

References

[1] A. Binley, "Tools and Techniques: Electrical Methods," *Treatise on Geophysics: Second Edition*, vol. 11, pp. 233–259, Jan. 2015, doi: 10.1016/B978-0-444-53802-4.00192-5.

[2] P. Hiskiawan, C.-C. Chen, and Z.-K. Ye, "Processing of electrical resistivity tomography data using convolutional neural network in ERT-NET architectures," *Arabian Journal of Geosciences*, vol. 16, no. 10, p. 581, Oct. 2023, doi: 10.1007/s12517-023-11690-w.

[3] I. V. Mel'nikova, "Regularization of ill-posed differential problems," *Siberian Mathematical Journal*, vol. 33, no. 2, pp. 289–298, Mar. 1992, doi: 10.1007/BF00971100.

[4] G. H. Golub, P. C. Hansen, and D. P. O'Leary, "Tikhonov Regularization and Total Least Squares," *SIAM Journal on Matrix Analysis and Applications*, vol. 21, no. 1, pp. 185–194, Jan. 1999, doi: 10.1137/S0895479897326432.

[5] S. Szalai, A. Novák, and L. Szarka, "Depth of Investigation and Vertical Resolution of Surface Geoelectric Arrays," *J Environ Eng Geophys*, vol. 14, no. 1, pp. 15–23, Mar. 2009, doi: 10.2113/JEEG14.1.15.

[6] K. Hellman, S. J. Johansson, P. O. Olsson, and T. D. Dahlin, "Resistivity Inversion Software Comparison," Sep. 2016. doi: 10.3997/2214-4609.201602016.

[7] Z. Wang, C. Sun, and D. Wu, "Near-surface Site Characterization Based on Joint Iterative Analysis of First-arrival and Surface-wave Data," Apr. 01, 2023, *Springer Science and Business Media B.V.* doi: 10.1007/s10712-022-09747-8.

[8] A. Yazdanpanah and M. Abedi, "Geophysical simulation of landslide model based on electrical resistivity and refraction seismic tomography through unstructured meshing," *International Journal of Mining and Geo-Engineering*, vol. 58, no. 3, pp. 263–270, 2024, doi: 10.22059/ijmge.2024.370406.595136.

[9] C. Rücker, T. Günther, and F. M. Wagner, "pyGIMLi: An open-source library for modelling and inversion in geophysics," *Comput Geosci*, vol. 109, pp. 106–123, Dec. 2017, doi: 10.1016/j.cageo.2017.07.011.

[10] K. Damavandi, M. Abedi, G. H. Norouzi, and M. Mojarab, "Geoelectrical modelling of a landslide surface through an unstructured mesh," *Bulletin of Geophysics and Oceanography*, vol. 63, no. 2, pp. 337–356, Jun. 2022, doi: 10.4430/bgo00384.

[11] A. DEY and H. F. MORRISON, "RESISTIVITY MODELLING FOR ARBITRARILY SHAPED TWO-DIMENSIONAL STRUCTURES*," *Geophys Prospect*, vol. 27, no. 1, pp. 106–136, Mar. 1979, doi: 10.1111/j.1365-2478.1979.tb00961.x.

[12] O. C. Zienkiewicz, D. W. Kelly, and P. Bettess, "The coupling of the finite element method and boundary solution procedures," *Int J Numer Methods Eng*, vol. 11, no. 2, pp. 355–375, Jan. 1977, doi: 10.1002/nme.1620110210.

[13] J. H. Coggon, "ELECTROMAGNETIC AND ELECTRICAL MODELING BY THE FINITE ELEMENT METHOD," *GEOPHYSICS*, vol. 36, no. 1, pp. 132–155, Feb. 1971, doi: 10.1190/1.1440151.

[14] C. Rücker, T. Günther, and K. Spitzer, “Three-dimensional modelling and inversion of dc resistivity data incorporating topography - I. Modelling,” *Geophys J Int*, vol. 166, no. 2, pp. 495–505, Aug. 2006, doi: 10.1111/j.1365-246X.2006.03010.x.

[15] T. Günther, C. Rücker, and K. Spitzer, “Three-dimensional modelling and inversion of dc resistivity data incorporating topography - II. Inversion,” *Geophys J Int*, vol. 166, no. 2, pp. 506–517, Aug. 2006, doi: 10.1111/j.1365-246X.2006.03011.x.

[16] A. S. Berahas, R. H. Byrd, and J. Nocedal, “Derivative-Free Optimization of Noisy Functions via Quasi-Newton Methods,” *SIAM Journal on Optimization*, vol. 29, no. 2, pp. 965–993, Jan. 2019, doi: 10.1137/18M1177718.

[17] N. Andrei, *Nonlinear Conjugate Gradient Methods for Unconstrained Optimization*, vol. 158. Cham: Springer International Publishing, 2020. doi: 10.1007/978-3-030-42950-8.

[18] G. Fasano, “Conjugate gradient (CG)-type method for the solution of Newton’s equation within optimization frameworks,” *Optim Methods Softw*, vol. 19, no. 3–4, pp. 267–290, Jun. 2004, doi: 10.1080/10556780410001689234.

[19] Y. Yuan, “Recent advances in trust region algorithms,” *Math Program*, vol. 151, no. 1, pp. 249–281, Jun. 2015, doi: 10.1007/s10107-015-0893-2.

[20] T. Steihaug, “The Conjugate Gradient Method and Trust Regions in Large Scale Optimization,” *SIAM J Numer Anal*, vol. 20, no. 3, pp. 626–637, Jun. 1983, doi: 10.1137/0720042.